CHAPTER 4

SYNTHESIS AND CHARACTERIZATION OF Ag-Cu AND Au-Cu ALLOY NANOPARTICLES

This chapter deals with green synthesis and structural characterizations of Ag-Cu and Au-Cu alloy NPs in two separate sections. After a brief introduction of phases stable under equilibrium and metastable conditions for these systems, experimental part pertaining to synthesis is given. Separate sections related to results and discussion are given for clarity of presentation. Conclusions drawn from the results obtained here are given at the end of this chapter.

4.1 The Ag-Cu alloy nanoparticles

4.1.1 Introduction

The optical and electronic properties of the alloy NPs can be very different from those of the elemental metal NPs. Synthesis of Ag-Cu alloy NPs received considerable attention owing to their potential applications in plasmonics, nano-electronics as interconnects, inkjet printings, catalysis, antimicrobial activities, and for die-attach [77, 116, 180–187]. Solution phase synthesis is preferred as this provides ease of control on morphology of the NPs, and scalability for NPs [185]. For the Ag-Cu alloy NPs syntheses in aqueous medium under ambient conditions have been reported by several research groups [72, 77, 78, 123]. The importance of working with Ag-Cu system draws impetus owing

to positive heat of mixing giving rise to very limited solubility at room temperature [17]. The equilibrium solid solubility of Cu in Ag is $\sim$ 13% at 1050 K while there is insignificant solubility of Ag in Cu (cf. Figure 1.4). Enhancement of solid solubility has been reported in both bottom up and top down approaches of Ag-Cu alloying [123, 187, 188]. Alloying of Ag-Cu was studied at different length scales and core-shell phase separated structures of Ag and Cu was also reported in literature [79, 184]. LSPR can be tuned over a range in between the individual components absorption peak by changing the proportion of Ag and Cu. In this section, wet chemical synthesis of the Ag-Cu alloy NPs stabilized by rice-starch in aqueous medium has been reported. Changing molar ratio of Ag and Cu precursors, varied degrees of solid solubilities in the Ag–Cu system are observed [77].The stability of Ag-Cu alloy sols is also studied here.

4.1.2 Experimental

The synthesis protocol requires 20 mL rice-starch (a detail of preparation of rice-starch has already been presented in chapter3). This was mixed with 20 mL (0.01M) $Cu(NO_3)_2.3H_2O$ aqueous solution under magnetic stirring. In this solution, 20 mL (1M) of hydrazine hydrate (HH) was added drop- wise. Various colours (henna, orange, light brown, and dark brown) were observed in the process of addition of HH. The resulting Cu NPs suspension was stirred for about 30 minute for the completion of reaction. This suspension was kept for 24 h in ambient condition. The dark brown colour changes to red brown. Another solution containing 20 mL (0.01M) $AgNO_3$ was added drop wise in the Cu NPs suspension for Ag-Cu alloy NPs formation. The initial red-brown colour changed gradually to

black- brown one. It was observed that precipitation was neither seen in the bottom nor on the side walls of the reaction flask. By changing the molar ratio of $AgNO_3$ with respect to $Cu(NO_3)_2.3H_2O$ (1:1,2:1,3:1,4:1, and 5:1), a series of Ag-Cu alloy NPs was synthesized. The Ag-Cu alloy NPs stabilized with rice-starch will henceforth be referred to as A1, A2, A3, A4, and A5. The Ag-rich and Cu-rich phases will be designated by (Ag) and (Cu) respectively. The Ag-Cu alloy NPs suspension stabilized with rice-starch were characterized with UV-Vis spectrophotometer (Perkin-Elmer XLS+) for the formation and stability of the sols by means of absorbance intensity and peak maxima. The Ag-Cu alloy nanopowders were obtained by centrifugation and ultra-sonication cycles. They were dispersed in ethanol with ultra-sonicator. A drop of these suspensions was coated on carbon coated nickel grid for TEM (FEI Tecnai G^2 T20 operating at 200 kV) investigations. The structure of the Ag-Cu alloy NPs was studied by XRD (Rigaku DMAXII with Cu-Kα as target material).The alloying behavior has been studied in detail by HRTEM. The chemistry of the grown Ag-Cu alloy NPs was investigated by HAADF- STEM- EDS.

4.1.3 Results and discussion

The XRD patterns for various rice-starch stabilized alloy NPs are shown in Figure 4.1. Table 4.1 summarizes the quantitative details of the XRD analysis. It has been known that the lattice parameters for elemental Ag and Cu are 4.086 Å (PDF card no. 01-073-6976) and 3.615 Å (PDF card no. 00-004-0836), respectively. The lattice parameters of the identified phases are compared with the experimental data of Linde [189]. In all the samples under investigation, besides the FCC phase, the hexagonal 2H-(Ag) phase is also

TABLE 4.1: Characteristics of the phases present, corresponding lattice parameters and the coherently scattered domain size of the rice-starch stabilized Ag-Cu alloy NPs.

Alloy designation (Ag:Cu) Molar ratio	**Phases observed (at.%)**	**d-spacing (Å)**	**lattice parameter (Å)**	**Coherently scattered domain size (nm)**
A1 (1:1)	2H-Ag fcc-Ag fccAg99.7Cu0.3 fccAg91.3Cu8.7	2.390 (0002) 2.366 (111) 2.358 (111) 2.340 (111)	- 4.09 4.084 4.052	- - $\sim$ 11 $\sim$ 18
A2(1:2)	2H-Ag fccAg99.7Cu0.3 fcc97.3Cu2.6 fcc93.1Cu6.9 fcc Ag93.1Cu6.9	2.389 (0002) 2.367 (111) 2.358 (111) 2.353 (111) 2.345 (111)	- 4.09 4.084 4.075 4.061	- - $\sim$ 11 - $\sim$ 16
A3 (1:3)	2H-Ag fccAg99.7Cu0.3 fccAg1.4Cu98.6 -	2.383 (0002) 2.359 (111) 2.092 (111)	- 4.085 3.623	- $\sim$ 10 -
A4 (1:4)	2H-Ag fccAg fcc95.6Cu4.4 fccAg1.4Cu98.6 -	2.370 (0002) 2.365 (111) 2.349 (111) 2.092 (111) 1.810 (200)	4.09 4.068 3.623	- $\sim$ 14 -
A5 (1:5)	2H-Ag fccAg94.3Cu5.7 fccAg89.4Cu10.6 fcc-Cu -	2.354 (0002) 2.346 (111) 2.336 (111) 2.079 (111) 1.801 (200)	4.063 4.046 3.600	- $\sim$ 15 $\sim$ 21

formed. The only reflection corresponding to (0002) plane of the 2H-(Ag) phase has been observed. The ICDD (PDF card No. 01-071-5025) d-value for this plane is $\sim$2.395Å. Similar values are reported for samples A1 and A2. However, from A3 onwards, the (0002) line 2H-(Ag) phase d-value demonstrates progressive decrease with increase in $Cu(NO_3)_2{\cdot}3H_2O$ proportion in the initial composition. This may be due to increasing alloying of the 2H-(Ag) phase. In A1, two FCC (Ag) (111) phases are formed with slightly

different degrees of alloying. Similarly, in sample A2, pure FCC Ag phase and other FCC (Ag) phases with increasing solubility of Cu phases are found. For samples A3, A4 and A5, although there is some solid solubility of Cu in FCC (Ag), no systematic increase in solubility with initial $Cu(NO_3)_2{\cdot}3H_2O$ proportion is observed. The maximum solubility of (about $\sim$11 at.%) Cu in FCC (Ag) is obtained in A5. In addition, peak corresponding to the pure FCC Cu is also observed.

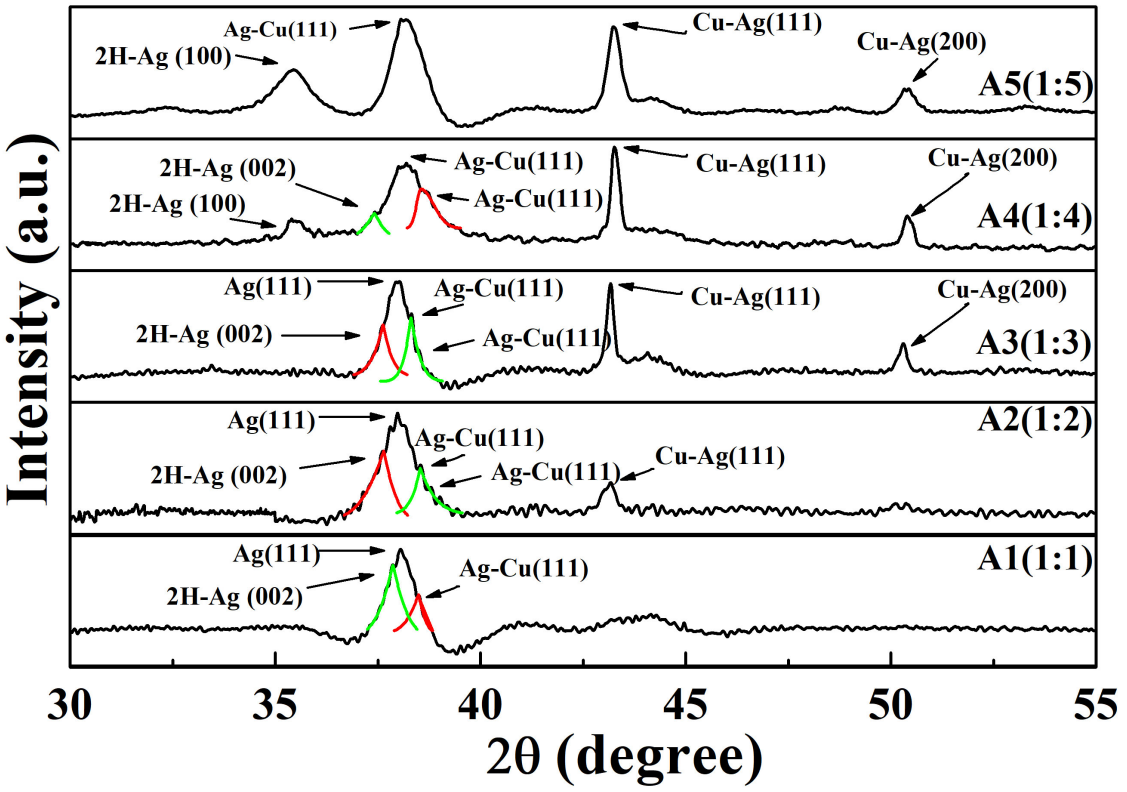

FIGURE 4.1: XRD patterns of rice-starch stabilized Ag-Cu alloy NPs

The representative bright field TEM micrographs, their corresponding SAD patterns, and size distribution histogram of Ag-Cu alloy NPs (A1, A3, and A5) are shown in Figure 4.2. The Ag-Cu alloy NPs showing ring patterns indicated crystalline NPs. The rings of A1 and A3 could be systematically indexed to those of FCC (Ag). The pattern

of A5 displayed reflection corresponding to (111) of FCC-(Cu) in addition to FCC-(Ag) rings. The observed SAD patterns of Ag-Cu alloy NPs may be explained as (1) HH acts as strong reducing agent for Ag^{+} that leads to higher nucleation rate of Ag and hence smaller size of FCC (Ag) NPs, and/or (2) FCC (Ag) NPs being smaller in size ($\sim$10 nm) as compared to Cu NPs (cf.Figure 4.2) dominates in TEM field of view.This results in FCC (Ag) ring pattern and shows a few spots corresponding to FCC (Cu) NPs. The particle

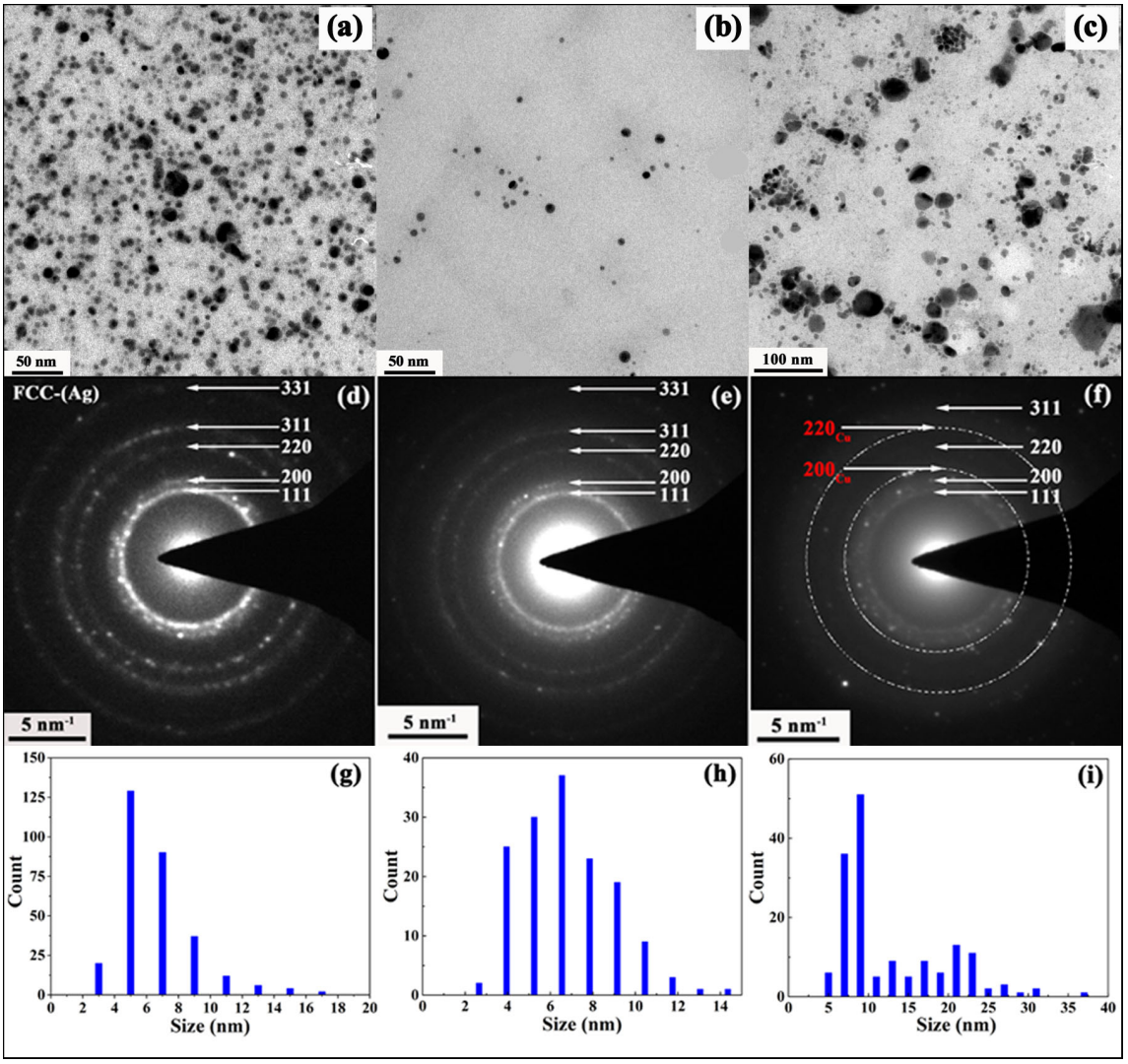

FIGURE 4.2: Representative TEM images of A1,A3 and A5 (a-c), corresponding SAD patterns (d-f) and size distribution histograms (g-i).

size distribution histograms (shown in Figure 4.2 (g-i)) were generated by counting more than 200 particles of Ag-Cu alloy NPs in a random field of view. The range of particle size of alloy NPs is given in the Table 4.2.

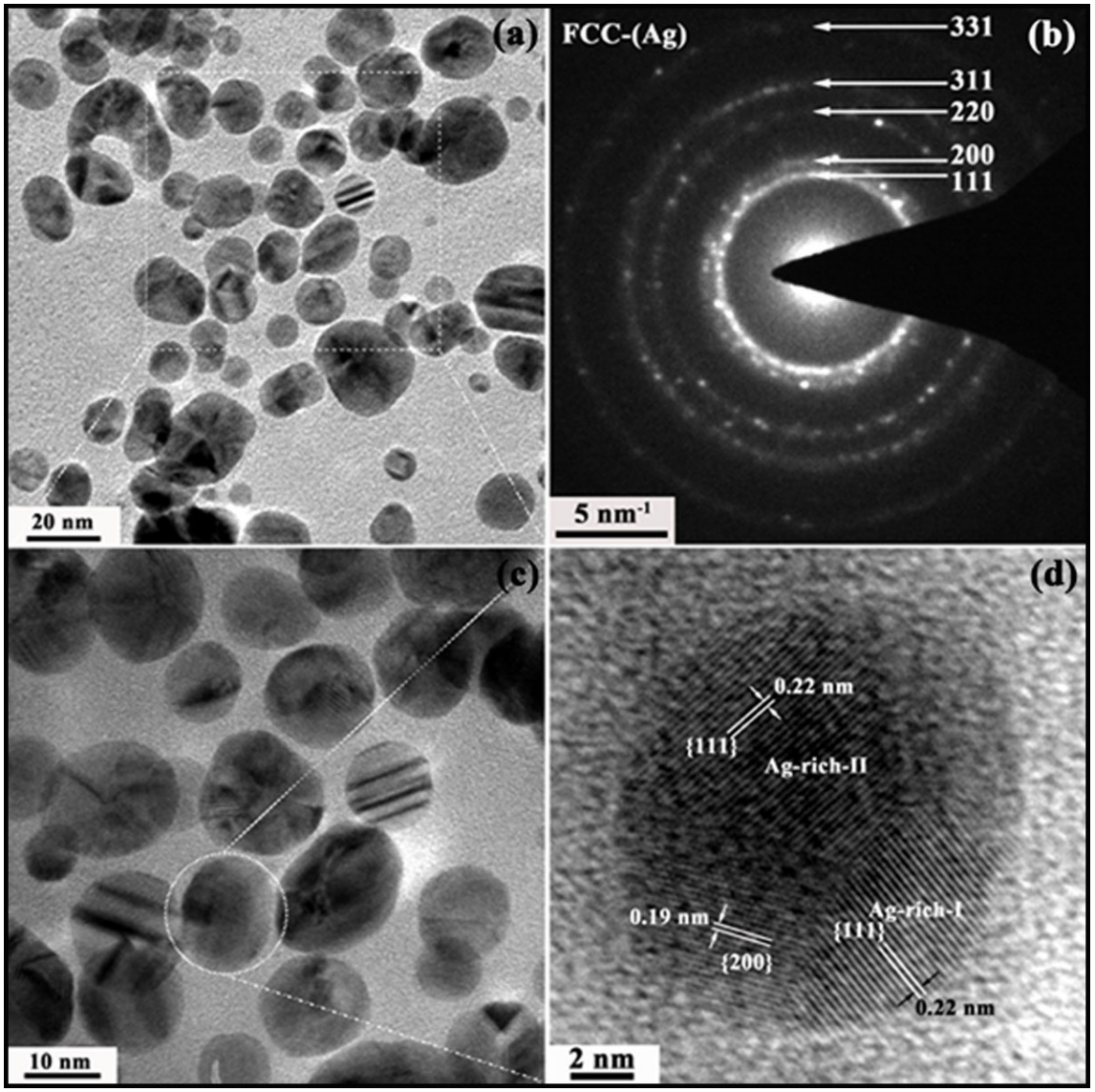

FIGURE 4.3: Representative TEM images (a), SAD pattern (b), magnified image (c), and HRTEM image of a particle showing domains with varied degree of solid solubilities (d) of Ag-Cu alloy NPs.

Alloying behavior of the Ag-Cu NPs have been studied in detail through TEM. For example, TEM images with varied magnification, SAD pattern, and HRTEM image

from a single particle is shown in Figure 4.3. The Ag and Cu in their bulk state possess d-spacing ∼2.08 Å and ∼2.36 Å corresponds to FCC-Cu (111) and FCC-Ag (111) respectively. The lattice fringe spacing measured from several HRTEM micrographs showed a range of the d-spacing values corresponding to Ag (111) (∼ 2.2 Å to 2.3 Å) and Cu (111) (∼ 2.0 Å to 2.1 Å) respectively. The HRTEM micrographs of different NPs of samples A1, A3, and A5 were captured and representative images are depicted in Figure 4.4 .These

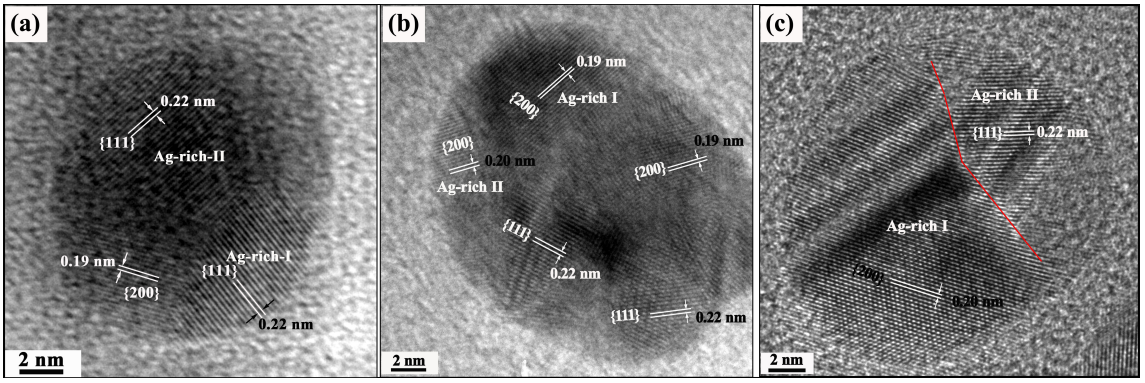

FIGURE 4.4: Representative HRTEM images from Ag-Cu alloy NPs of samples A1(a), A3(b), and A5 (c) respectively. The lattice fringe spacing corresponding to Ag-rich phases are depicted.

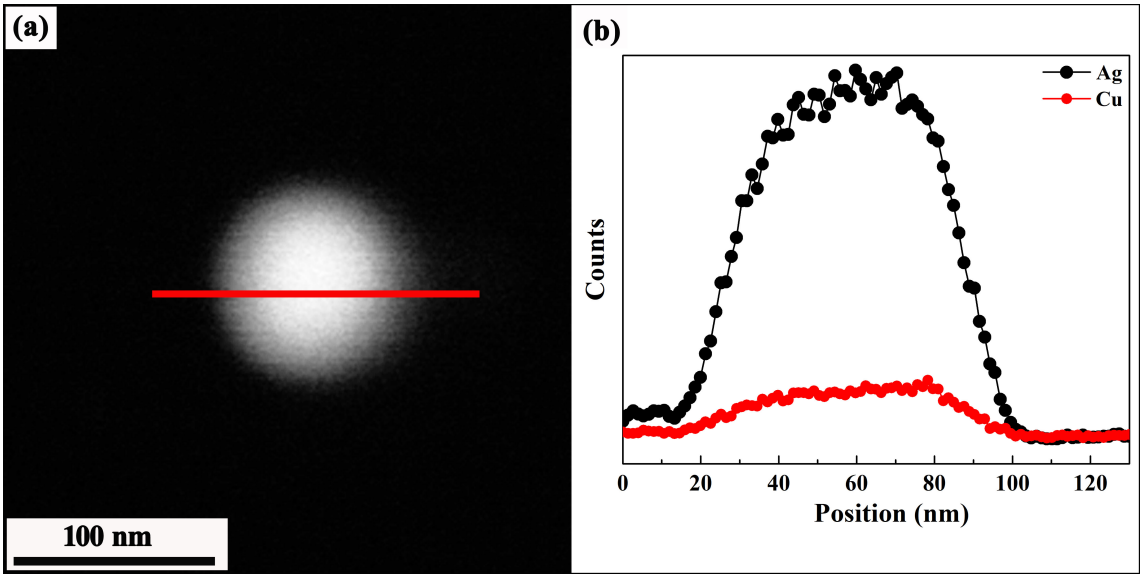

FIGURE 4.5: HAADF-STEM-EDS elemental line scan from a single particle from alloy A1. The HAADF image (a) and Ag, Cu line profiles (b) of a single particle.

changes in the observed d-spacing compared to their elemental counterparts suggest the formation of solid solution of FCC (Ag) and FCC (Cu). This further substantiates our finding based on XRD analysis. The chemistry of alloy NPs is investigated with HAADF-STEM-EDS. The line scan along a single particle of sample A1 is shown in Figure 4.5. The uniform profiles of Ag and Cu suggests that Ag-Cu alloying has taken place. The HAADF-STEM-EDS elemental maps of Ag and Cu from sample A3 is depicted in Figure 4.6. The uniform distribution of Ag and Cu throughout the particles revealed Ag-Cu alloyed NPs. It may as well be argued that the alloying has not taken place instead Cu is sitting on Au as a layer or vice-versa. This postulate could be ruled out through the analysis of high resolution TEM images where the images have been quantitatively analyzed to have formed crystalline nanoparticles with specific structure and lattice parameter. In case

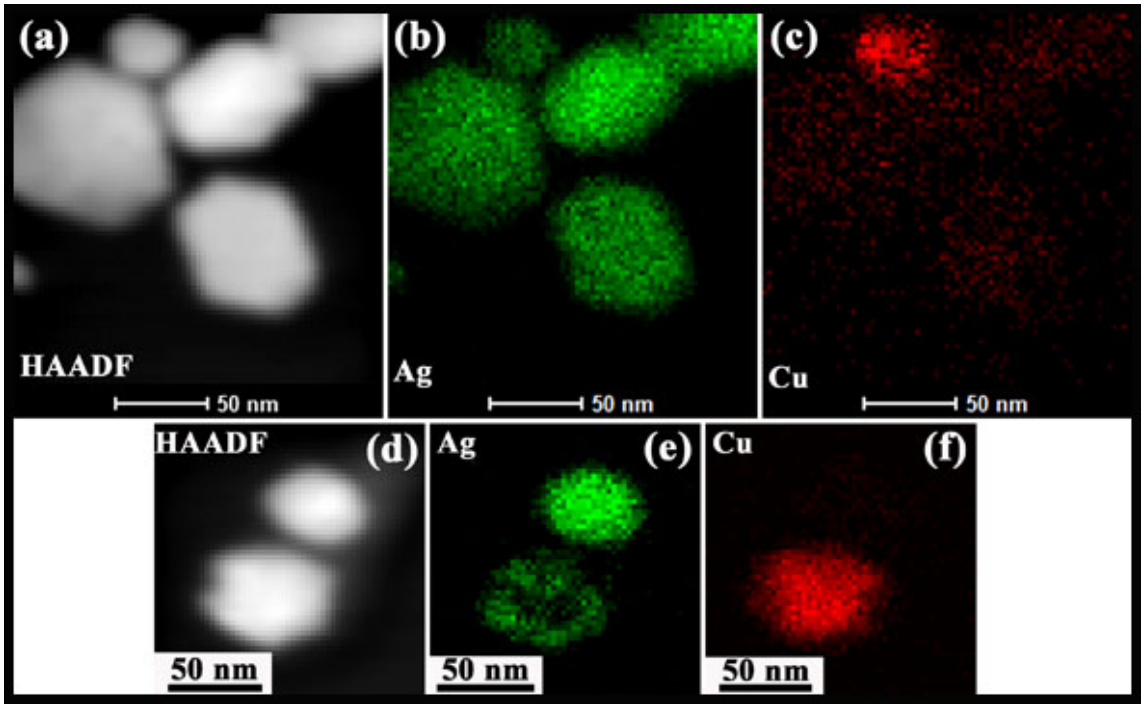

FIGURE 4.6: HAADF-STEM-EDS elemental maps of Ag and Cu from alloy A3 from two different regions.

of formation of bilayers, existence of Moiré patterns would have been a definite possibility which is not seen in the present case. Additionally, Ag-rich and Cu-rich NPs can be seen in the maps (Figures 4.6 b and c). Moreover, Cu-core and Ag-shell NPs has also been observed based on Cu and Ag concentration as shown in Figures 4.6 (e) and (f). Figure 4.7 shows line profiles of Ag and Cu of two particles of sample A5. The elemental profiles show that one particle is rich in Ag (top Figure 4.7 a) and another in Cu (bottom of Figure 4.7 a). The profiles of Cu in Ag-rich and that of Ag in Cu-rich particles are non-uniform. This suggests a clustering tendency of Cu and Ag in the Ag-rich and Cu-rich particles, respectively. From the TEM and HAADF-STEM-EDS results, it has been confirmed that Ag-Cu alloy NPs have formed. Additinally, signatures of Cu-Ag core-shell NPs are also observed.

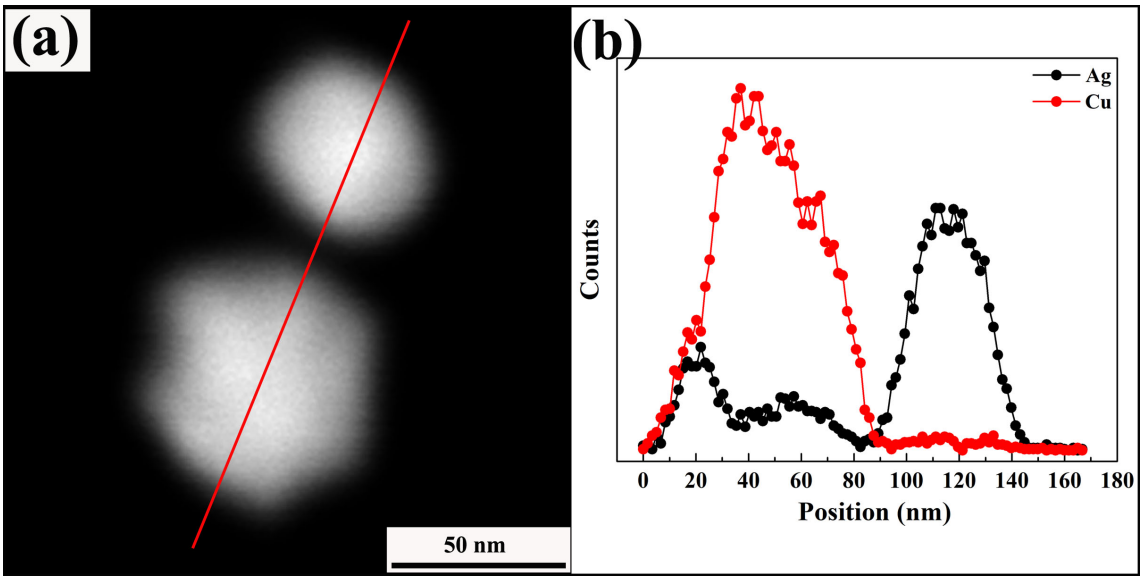

FIGURE 4.7: HAADF-STEM-EDS elemental line scans from two particles from alloy A5. The HAADF image (a) and Ag, Cu line profiles (b) of from particles.

4.1.4 LSPR behavior of Ag-Cu alloy NPs

It is important to mention that LSPR of metal NPs is a phenomenon which depends on shape and size of the NPs as well as on refractive index of the stabilizer used to stabilize NPs. The electron scattering enhancement at the surfaces of NPs owing to decreased particle size leads to increase in absorbance bandwidth [116]. Hence, variations in bandwidth ($\Delta\lambda$) and shifts in resonance peak (λ_{max}) are important parameters in characterizing the metal NPs. UV-Vis absorbance spectra of Cu NPs stabilized rice-starch shows LSPR absorbance peaks (λ_{max}) $\sim$ 584 nm. These observed λ_{max} are in the range of characteristic LSPR peak of Cu NPs [190]. In the present synthesis conditions, excess hydrazine hydrate present in the Cu NPs suspension is capable of reducing Ag^{+} ions to Ag, which may produce phase separated Ag NPs. Moreover, Ag NPs may nucleate on pre-existing Cu NPs surface and oxidise Cu NPs as a result of galvanic replacement reaction [79]. One Cu^{2+} ion would be released into the suspension after 2 Ag^{+}ions reduction in the galvanic replacement reaction. This decreases the size of the Cu NPs and a blue shift in LSPR curve is expected. The experimentally observed LSPR absorbance curves of rice-starch stabilized Ag-Cu NPs are shown in Figure 4.8. The absorbance spectra were de-convoluted after necessary base line correction to get λ_{max} and $\Delta\lambda$ corresponding to Ag NPs, Cu NPs and Ag-rich NPs for samples A1-A5, is given in Table 4.2. The de-convoluted LSPR curves of the sample A1, for example, is depicted in Figure 4.8(b). The Cu-rich NPs absorbance could not be de-convoluted from experimental LSPR curves. The nature of deconvoluted LSPR curve corresponding to Ag NPs in samples, as concentration of $AgNO_3$ decreases from A1 to A5, the λ_{max} increases from 378 to 394 nm suggesting a red shift with a little

increase in $\Delta\lambda$. This red shift may be attributed to higher nucleation rate of Ag NPs in A1 and decreases with decrease in $AgNO_3$ concentration from A1 to A5. The λ_{max} values for Cu NPs show red shift (532-583 nm) whereas $\Delta\ \lambda$ decreases (170- 49 nm) with decreasing $AgNO_3$ concentration from A1 to A5. This red shift may be ascribed to suppressed galvanic replacement reaction of Ag^+ on preexisting Cu NPs surfaces. The decreased $\Delta\lambda$ suggest less polydispersity in Cu NPs, may result from reduced etching of Cu NPs by Ag^+ with decreased $AgNO_3$ concentration. In the case of (Ag) NPs, λ_{max} values are found to be red shifted with increased LSPR peak widths compared to that of Ag NPs. The maximum red shift of 79 nm and minimum of 55 nm have been observed in samples A5 and A1, respectively. This suggests probability of Ag-Cu alloy NPs formation in A5 is more than that of the rest. The maximum solid solubility of Cu in Ag ($\sim$11at. %) in A5 is obtained from XRD results. Despite absence of (Cu) NPs LSPR curves in de-convoluted spectra, it is to be noted that peak widths $\Delta\lambda$ (170 to 49 nm) corresponding to Cu NPs in all the samples is more than in pure Cu NPs (42 nm). This broadening in LSPR curve is suggestive of Ag-Cu alloy NPs. In the de-convoluted LSPR curve of A1, a curve with λ_{max} value 690 nm with $\Delta\lambda \sim 260$ nm is also obtained. This may be due to the oxidation of Cu^{2+} released in the process of galvanic replacement reaction of Ag^+ and Cu NPs. The solid solubility of Cu in Ag and vice versa based on XRD could be correlated with LSPR curves for Ag-Cu alloy nanoparticles.

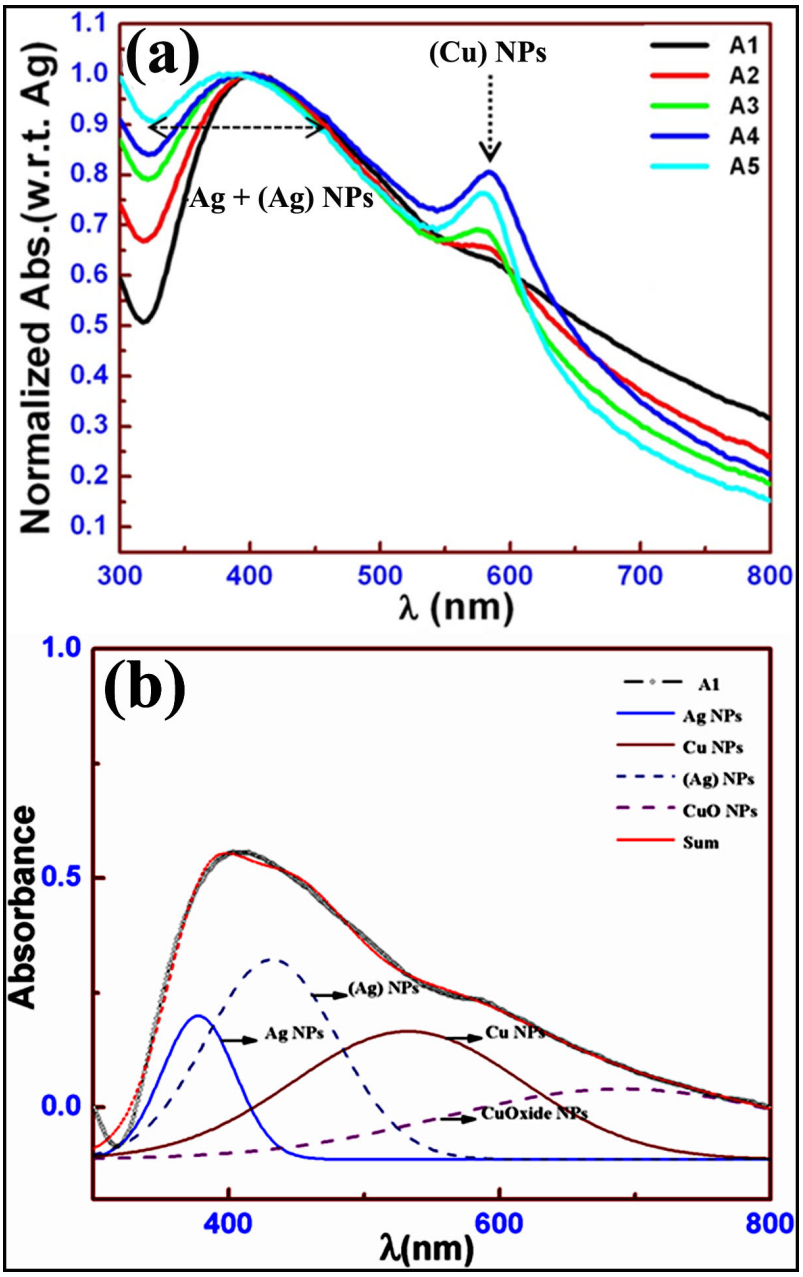

FIGURE 4.8: UV-Vis absorbance spectra of Ag-Cu alloy sols displaying LSPR peaks corresponding to Ag-rich and Cu-rich NPs (a) and deconvoluted spectrum of alloy A1 showing absorbance corresponding to Ag NPs, (Ag) NPs, Cu NPs and copper oxide NPs respectively(b).

TABLE 4.2: Summary of the Ag-Cu alloy NPs characteristics.

Alloy designation	**Deconvoluted LSPR wavelength maxima (λmax) and FWHM $\Delta\lambda$ (nm)**						**UV-Vis evolution studied for 77 days**		**TEM particle size range (nm)**	**Solid Solubility based on XRD (atom %)**	
(Ag:Cu) Molar ratio	**λmax Ag**	**$\Delta\lambda$**	**λmax (Ag)**	**$\Delta\lambda$**	**λmax Cu**	**$\Delta\lambda$**	**λmax (Ag)**	**λmax (Cu)**		**(Ag)**	**(Cu)**
A1 (1:1)	378	54	532	170	431	96	408- 411	——	3.0- 17.0	8.70	-
A2 (1:2)	382	66	577	100	447	102	409- 411	562-565	——	6.89	-
A3 (1:3)	386	58	580	77	455	97	409- 412	565-572	3.0- 14.0	0.3	1.46
A4 (1:4)	390	56	588	75	462	94	404- 412	566-574	——	4.48	1.45
A5 (1:5)	394	66	583	49	473	114	404- 414	573-580	5.0- 37.0	10.51	-

4.1.5 Stability of Ag-Cu alloy NPs

Metal nanoparticle dispersions, because of their high surface energy, are inherently unstable with respect to aggregation, which causes the precipitation. Capping these nanoparticles with a monolayer of any selected molecules is a convenient way to stabilize them not only with respect to aggregation but also against chemical reactions. The general stabilization mechanisms of colloidal materials have been described in the Derjaguin–Landau–Verwey–Overbeek (DLVO) theory [191]. At short interparticle distances, two particles are attracted to each other by van der Waals forces in the absence of repulsive forces. Such an attractive force depends inversely as a sixth power of distances between their surfaces. In absence of the repulsive forces, metal nanoparticles will agglomerate. Consequently, the stability of suspensions of nanoparticles in a liquid medium is ensured by the repulsion between the particles. There are two general way of stabilization of metal nanoparticles viz., electrostatic and steric mechanisms. The stability of the sol has been assessed with visual observation of the sol colour as well as with the sedimentation as a result of agglomeration. Experimentally, UV-Vis absorbance maxima (λ_{max}) with respect to time have been utilized as a gauge associated with the stability of the sol [191]. Evolution of the UV-Vis absorbance spectra of Ag-Cu alloy NPs was studied up to 77 days. The extent of shift in λ_{max} is summarized in Table 4.2. The profiles of the absorbance curves show indication of slight shifts (both red and blue) in the absorbance peaks as shown in Figure 4.8. They further substantiate claim of this investigation of sol stability against agglomeration and/or dissolution of the NPs as a concurrent process with respect to time.

4.2 The Au-Cu alloy nanoparticles

4.2.1 Introduction

As mentioned in section 4.1.1, the control of shape, size, chemistry and structural stability at nanoscale is of paramount importance for applications [10, 125, 192]. Some of the issues pertaining to above controls for Ag, Au, Cu nanoparticles and their alloys has received considerable attention for their optical and catalysis applications [192, 193]. Phase stability of these alloy nanoparticles cannot be understood based on information contained in equilibrium phase diagram. Such a phase diagram does not include size of the system as a parameter to investigate the various phase fields. This aspect needs to be explored before a reproducible behavior of the system during usage is realized. Reports on such investigations are not readily available in literature. The phase diagram of Au-Cu is complex in nature with phase fields containing several intermetallics like Au_3Cu, AuCu and $AuCu_3$ at lower temperatures ($\sim$ 400 ºC) [80]. Although considerable amount of work has been done in the area of Au-Cu alloy nanoparticles with respect to syntheses, characterization and their applications but structural investigations near intermetallic phase fields have received lesser attention. The formation of new phases in Au-Cu nanoparticles have been demonstrated which are not expected in the equilibrium phase diagram (chapter 7). Therefore, objective of this part of the work is to study morphological and structural transformations in Au-Cu nanoparticles before and after heat treatment at $\sim$ 400 ºC. Such a temperature has been chosen to assess most of the phase fields reported in the phase diagram. It will be demonstrated that change of synthesis conditions and heat treatment

can give rise to formation of newer phases.

4.2.2 Experimental

4.2.2.1 Synthesis of Cu nanoparticles

Fifty mL aqueous solution of starch was prepared and 48 mg Cu $(NO_3)_2$. $3H_2O$ was mixed with the help of magnetic stirrer at room temperature. Thereafter, 1.0 mL of (0.1M) NaOH solution was added to the above solution. Drop wise addition of 2.0 mL (99 wt. %) hydrazine hydrate resulted in red brown color suspension of Cu NPs. This suspension was left at room temperature for about 24 h.

4.2.2.2 Synthesis of Au-Cu alloy nanoparticles

Ten mL of as prepared Cu NPs suspension was taken and diluted four times with deionized water. Thereafter, in each 10 mL of diluted Cu NPs suspension, required millimole of $HAuCl_4.3H_2O$ was added to make precursor ratio of Au and Cu to conform to 3:1, 1:1, and 1:3, respectively.

4.2.2.3 Characterization of Au-Cu alloy nanoparticles

The Au-Cu sols thus obtained were used to study their LSPR behavior. For TEM investigations, samples were centrifuged at 1000 RPM and washed twice with ethanol and dried in vacuum oven at 60 ^oC to get nanopowders. The powder thus obtained was used for heat treatment in N_2 medium. For TEM study, powder was dispersed in ethanol and a drop was transferred to a carbon coated nickel grid. The localized surface plasmon resonance

TABLE 4.3: LSPR maxima, FWHM, Zeta potential and particle size of the samples characterized in colloidal state.

Sample	**Absorbance maxima (λ_{max}) (nm)**	**FWHM (nm)**	**Zeta Potential (mV)**	**Particle diameter (nm)**	**Polydispersity index (PDI)**
Cu	569	48	—	—	—
Au:Cu (1:3)	565	85	+18	272	0.18
Au:Cu (1:1)	559	107	-43	102	0.40
Au:Cu (3:1)	558	107	+14	654	0.60

(LSPR) behavior of Au-Cu sols was studied by UV-Vis absorbance spectra. Mechanisms of growth at atomic level have been studied through high resolution phase contrast microscopy (HR-TEM). The Au-Cu nanopowders were obtained by centrifugation and ultrasonication cleaning cycles followed by drying in vacuum at 60 ^{o}C. To investigate the phase transformations in Au-Cu, the nanopowders were heat treated at $\sim$ 400 ^{o}C for 1 h in N_2 medium. The annealed nanopowders were investigated by TEM and STEM-EDS for their structural and chemical composition analyses. Nano-beam diffraction (NBD) patterns were acquired to probe the local structures of post-heat treated samples. The exposure time of CCD was kept $\sim$1.5 sec while recording the NBD patterns to minimize drift.

4.2.3 Results and discussion

4.2.3.1 LSPR behavior of Au-Cu alloy NPs

The UV-Vis absorbance spectra of Au-Cu (3:1), Au-Cu (1:1), Au-Cu (1:3), and Cu nanoparticles is depicted in Figure 4.9. The appearance of LSPR bands with absorbance maxima

at $\sim$ 569 nm corresponds to Cu NPs [79]. The Au-Cu alloy NPs with precursors mole ratio (3:1), (1:1), and (1:3) revealed the LSPR peak positions (λ_{max}) at around 558, 559, and 565 nm, respectively. The LSPR peak position values of Au-Cu alloy NPs were observed to lie in between Au and Cu NPs peak values. Moreover, the broadening of LSPR bands of Au-Cu alloy NPs was observed to be significantly more than that of Cu NPs. The LSPR bands of Au-Cu (3:1), Au-Cu (1:1) and Au-Cu (1:3) displayed broadening (FWHM) of $\sim$ 107 nm, 107 nm and 85 nm, respectively, compared to $\sim$ 48 nm of Cu NPs. The polydispersity index (PDI) values measured with dynamic light scattering (DLS) were found to be $\sim$ 0.60, 0.40 and 0.18 for these samples. These results will be discussed after presenting TEM results in the following section.

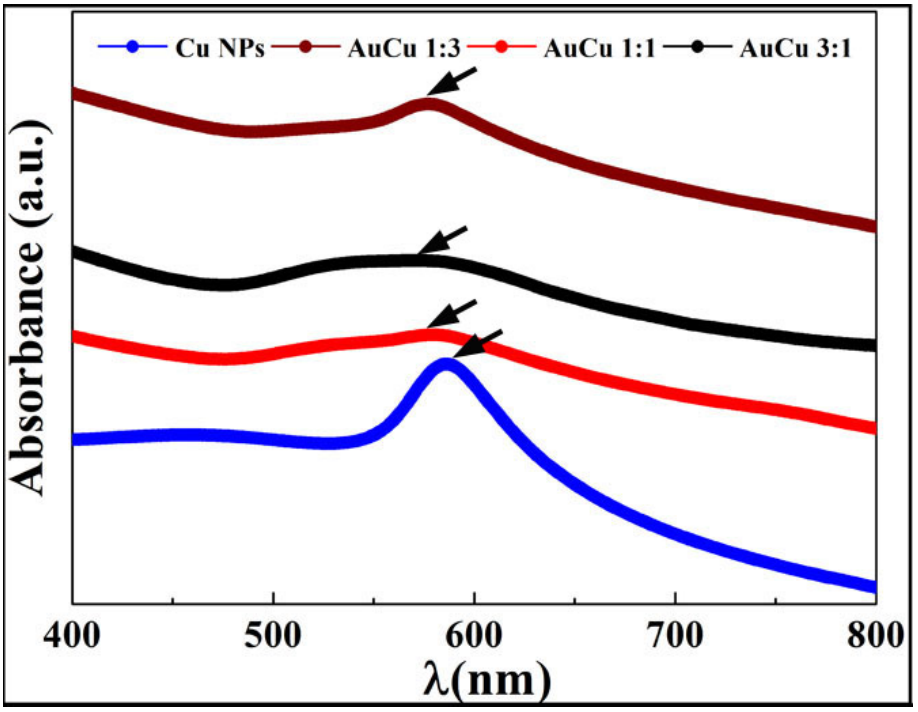

FIGURE 4.9: UV-Vis absorbance spectra corresponding to Cu, Au-Cu (1:3), Au-Cu (1:1) and Au-Cu (3:1) nanoparticles.

4.2.3.2 Structural and microstructural studies of as-synthesized Au-Cu alloy NPs

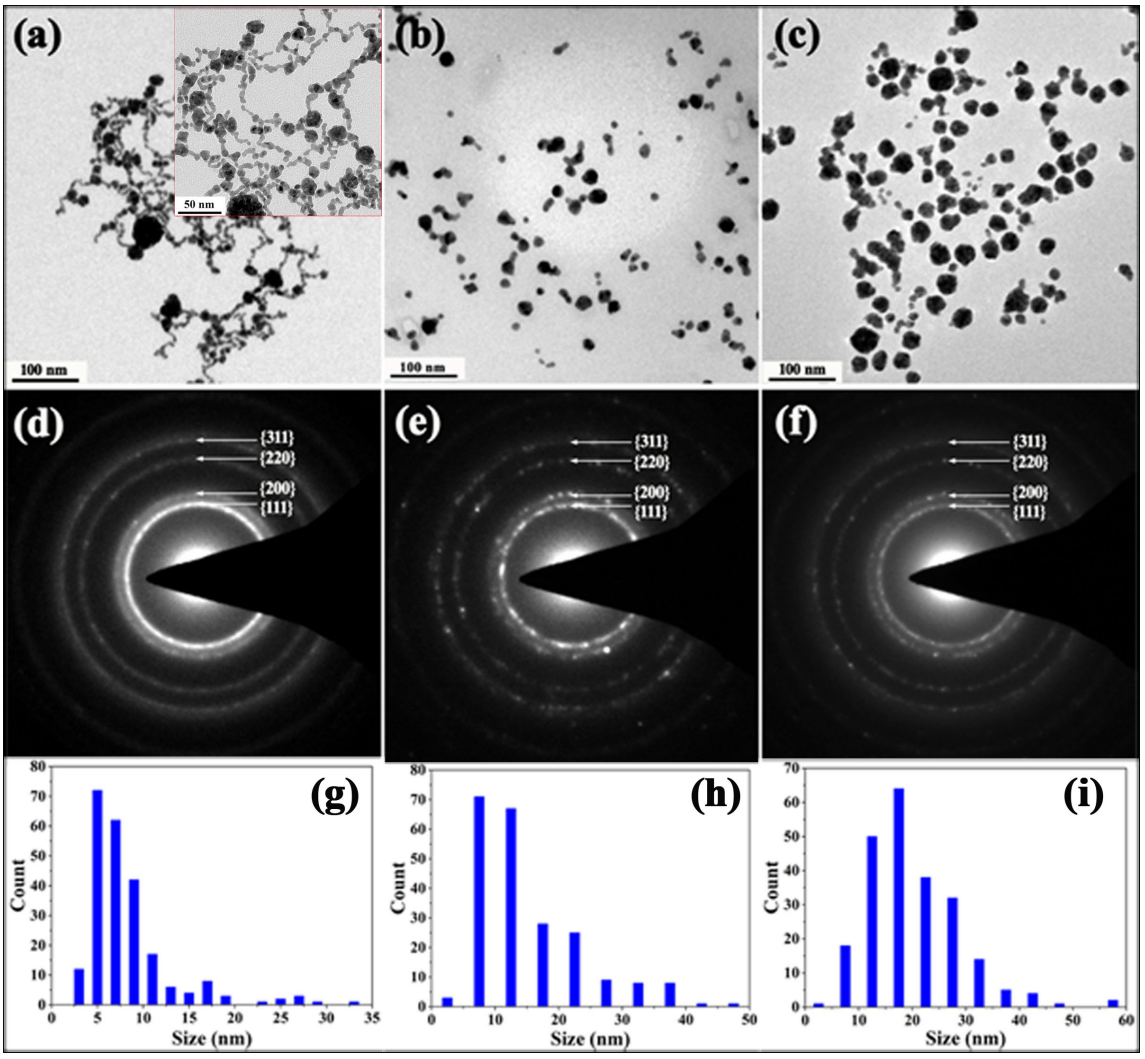

FIGURE 4.10: Representative BF TEM images (a-c), corresponding selected area electron DPs (d-f) and size distribution histograms (g-i) of Au-Cu (3:1), Au-Cu (1:1) and Au-Cu (1:3) samples.

Figure 4.10 shows bright field TEM micrographs, selected area diffraction (SAD) patterns and size distribution histograms of the samples Au-Cu (3:1), Au-Cu (1:1), and Au-Cu (1:3). The branched nanowire like morphology was observed for Au-Cu (3:1) sample which comprised of interconnected nanoparticles (nano-chains) of median size $\sim$ 5 nm. The isolated particles with size ranging from 15-25 nm were also observed (TEM

micrographs utilized for particle size measurements are shown in Figures A.3 (a-c) of Appendix A). The rings in the SAD pattern was indexed as those of a FCC crystal with a lattice constant of $\sim$ 0.40 nm conforming to the formation of a single phase solid solution. According to the table of Au solid solution lattice spacing as a function of composition [194], the composition of the Au-Cu solid solution with this lattice constant is Au-30 at. % Cu. The Au-Cu (1:1) sample displayed mostly particles with median size $\sim$ 12 nm together with a few linearly interconnected particles and agglomerated cluster of particles (TEM micrographs utilized for particle size measurements are shown in Figures A.3 (d-f) of Appendix A). The SAD pattern was indexed based on FCC crystal with a lattice constant of $\sim$ 0.39 nm. The BF TEM micrograph of Au-Cu (1:3) comprised of highly agglomerated particles with median size $\sim$ 19 nm with no sign of networking or branching. The SAD pattern was indexed with the help of FCC phase having lattice constant of $\sim$ 0.39 nm. The nanowire like morphology observed in the case of Au-rich sample need to be explored further. To probe the atomistic origin of growth of nanowire networks in Au-Cu (3:1) sample, HR-TEM micrograph from a section of nanowire network is presented in Figure 4.11. Two crystals were found to be attached with each other along $\{111\}$ through twin boundary (TB). The $\sim 141^o$ angle across the TB indicates that the NPs were attached via $\{111\}$ facets. The inset shows the FFT from the selected regions (shown as square boxes) which are oriented close to $< 011 >$ zone axes. Comparing with the $\{111\}$ facets, the $\{100\}$ facets of FCC metals were reported to have lower atomic density and more open sites that is beneficial for adsorption of surfactant molecules [195].Therefore, it seems that under the present synthesis condition, rice-starch preferentially adsorbed on

the $\{100\}$ facet, rendering NPs capable of attaching to each other via the less covered $\{111\}$ facets to form nanowires.

The morphologies observed with TEM can be correlated with characteristics measured in sol state. The polydispersity index (PDI) measured with dynamic light scattering (DLS) is given in Table 4.3. The Au-Cu (3:1) samples displayed the nanowire networks which is interconnected networks of particles of median size $\sim$ 5 nm which is akin to linear aggregation of particles. In the Au-Cu (1:1) this aggregation tendency is lesser compared to that of the Au-Cu (3:1) case. The PDI indices for these sols were found to be $\sim$ 0.60 and 0.40, respectively and is in conformity with TEM results. The Au-Cu (1:3) however, showed normal distribution of particles with average size $\sim$ 19 nm in conformity with the PDI values of 0.18.

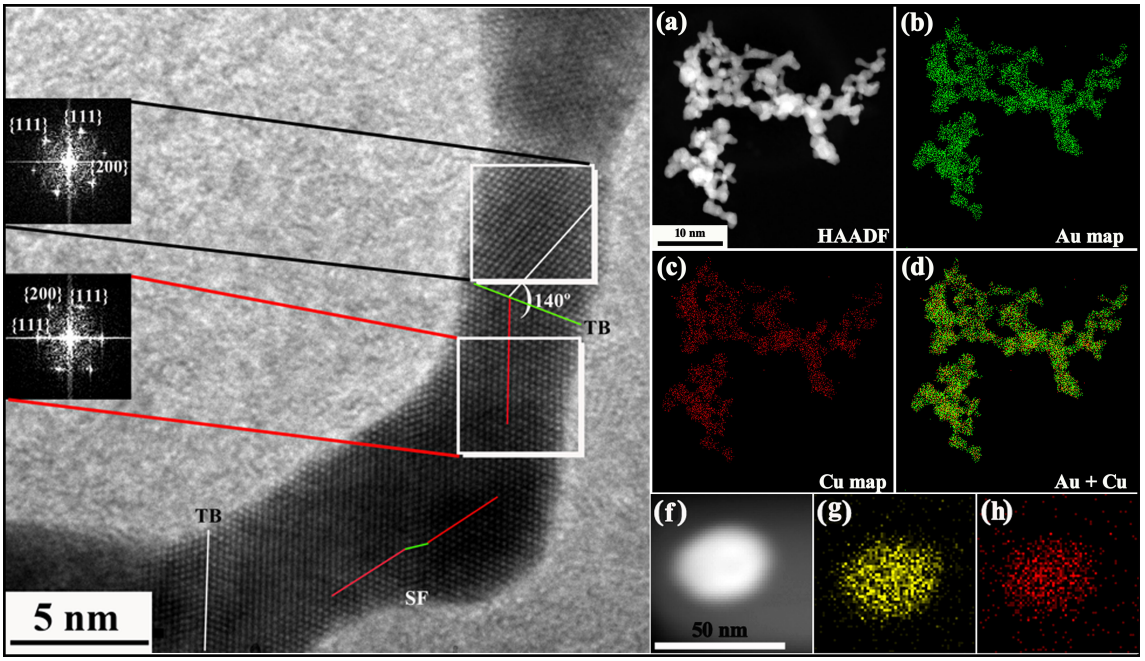

FIGURE 4.11: HRTEM image from a section of nanowire (left) where twin boundary (TB) and stacking fault is depicted. The STEM-HAADF-EDS elemental maps of nanowire networks and a single particle from Au-Cu (3:1) (a-d) and Au-Cu (1:3) (b-h) samples.

4.2.3.3 Chemical Analyses using STEM-HAADF-EDS

The STEM-EDS results show elemental composition of Au in Au-Cu (3:1), Au-Cu (1:1), and Au-Cu (1:3) as $\sim$ 66 at.%, 65 at.%, and 57 at.% respectively. The Cu content in the samples were quantified as $\sim$ 34 at.%, 35 at.%, and 45 at.%, respectively. The statistics are generated by averaging the data obtained by sampling at least from ten different regions. The EDS quantification has been done based on relative intensities of Au and Cu. In addition, the interaction volume for Au is more than that of Cu owing to higher atomic number of Au. The local chemistry at particle level might differ but the average chemistry of ensemble may be same. Figures 4.11 (b) – 4.11 (d) and 4.11 (f) – 4.11 (h) depict representative STEM-HAADF-EDS elemental maps corresponding to Au and Cu for samples Au-Cu (3:1) and Au-Cu (1:3), respectively. The maps display the homogeneous distribution of Au and Cu throughout the nanowires network and a nanoparticle from the samples Au-Cu (3:1) and Au-Cu (1:3), respectively. The TEM and STEM results show that alloy formation of Au-Cu has taken place. The lattice constants of FCC-AuCu alloy nanoparticles was derived by invoking Vegard's law [151] and estimated as 0.40 nm, 0.40 nm, and 0.39 nm corresponding to Au-Cu (3:1), Au-Cu (1:1), and Au-Cu (1:3) respectively. Having characterized them, these samples were heat treated at $\sim$ 400 °C for 1 h. Structural and microstructural characteristics of heat treated samples will be presented in the next section.

4.2.3.4 Structural investigation of heat treated Au-Cu alloy nanoparticles

Figure 4.12 displays the representative BF micrograph (Fig. 4.12 (a)) and NBD patterns from three different particles (cf. Fig. 4.12 (b), (c) and (d)) of (3:1) sample. The agglomerated particles with irregular shapes and crystals with extended sizes were observed in

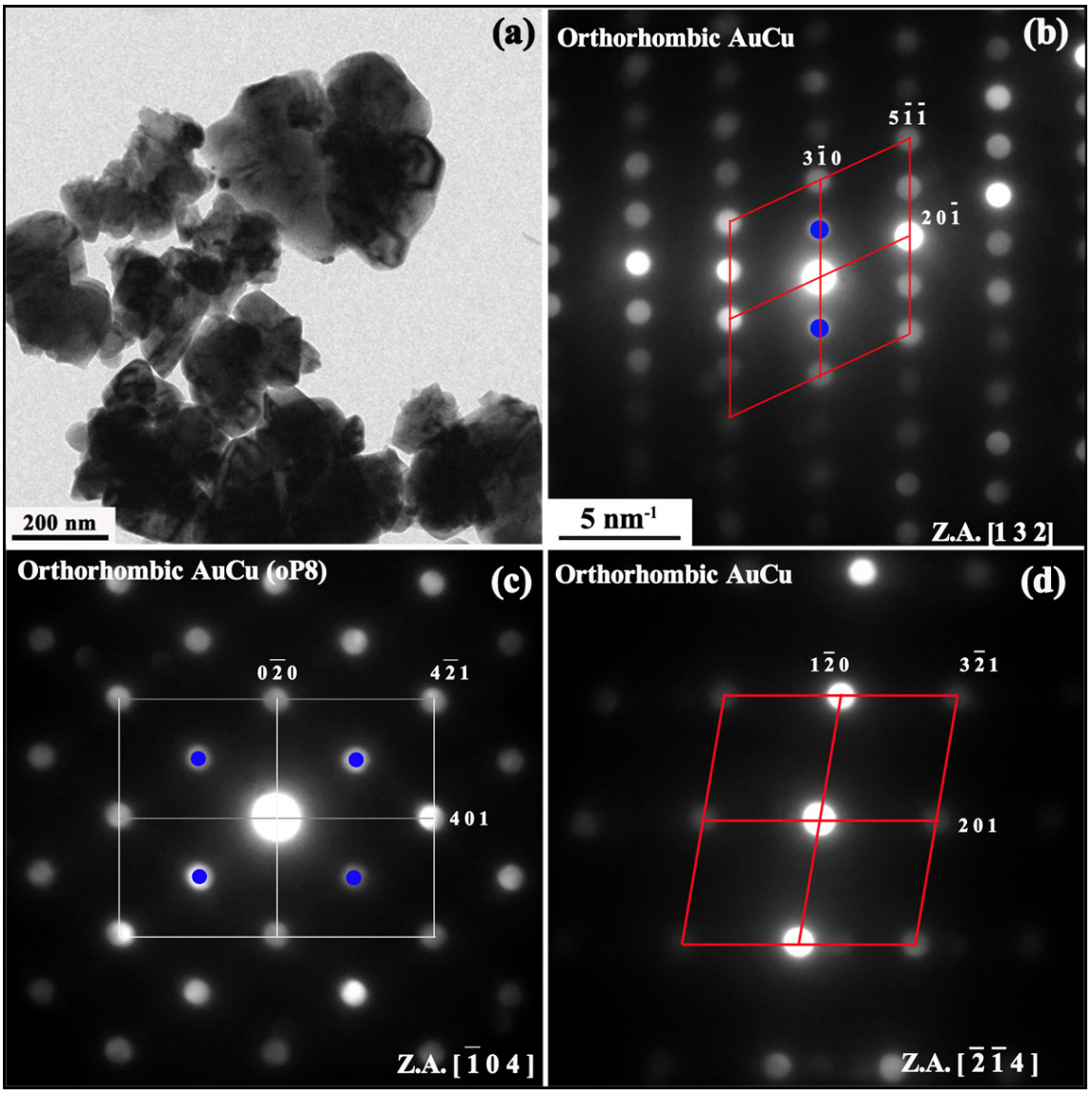

FIGURE 4.12: Representative BF TEM micrograph (a) and NBD patterns acquired from three different regions (b-d) of Au-Cu (3:1) sample. Blue filled circles showing superlattice spots and unindexed spots respectively in Figures (b) and (c), indexed based on orthorhombic AuCu (oP8) along [132] and [$\bar{1}$04] zones. Figure (d) shows NBD and spots could be indexed as those of orthorhombic AuCu (oP8) phase along [$\bar{2}\bar{1}$4] zone axis.

BF TEM image. The spots in NBD patterns shown in Figures 4.12 (b), (c) and (d) could be indexed to as those of orthorhombic AuCu (oP8) (ICDD card no. 00-038-0741) with lattice constants [a = 8.92 Å, b = 4.56 Å and c = 2.83 Å] oriented along [132], [$\bar{1}$04] and [$\bar{2}\bar{1}$4] zone axes respectively. The doubling of cell along [3$\bar{1}$0] has also been observed and indicated by a blue dot in Figure 4.12 (b). The closer spots highlighted with blue filled circles in the NBD pattern shown in Figure4.12 (c) could not be indexed with orthorhombic oP8 AuCu (details to be presented later in this section).

Figure 4.13 depicts the representative BF micrograph (Fig. 4.13 (a)) and three important NBD patterns from single particles (Figs. 4.13 (b), (c) and (d)) of Au-Cu (1:1) sample. The morphology observed is similar to that of Au-Cu (3:1) (cf. Fig. 4.12(a)). The NBD patterns shown in Figures 4.13 (b) and (c) could be systematically indexed to those of the ordered orthorhombic (oP8) AuCu structure oriented along [$\bar{1}$20] and [$\bar{1}$32]zone axes respectively. In addition, doubling of cells along [210] and [201] directions are also observed (spot encircled with blue color and a blue spot is shown in Figs. 4.13 (b) and (c) respectively). The NBD presented in Figure 4.13 (d) could be indexed with orthorhombic AuCu cell oriented along [$\bar{2}$14] zone axis.

Representative BF TEM image and NBD patterns of Au-Cu (1:3) is shown in Figure 4.14. The BF TEM image displays agglomerated morphology accompanied with particles having bigger size (Fig. 4.14 (a)). The NBD patterns shown in Figures 4.14 (b) and (c), phases were found to be AuCu orthorhombic (oP8) oriented along [$\bar{2}$14] and ordered cubic $AuCu_3$ (cP4) oriented along [1$\bar{1}$2] with lattice constants, a = 8.92 Å, b = 4.56 Å, c = 2.83 Å for AuCu and 3.75 Å for $AuCu_3$ respectively (ICDD card no. 00-035-1357).

The NBD pattern shown in Figure 4.14 (d) could be indexed with the help of orthorhombic (oP8) cell along [010] zone axis with some missing reflections such as $00\bar{1}$ and 200. They suggest that cell sizes along [100] and [001] has become half compared to that of standard oP8 AuCu structure (details are given later in this section). The experimentally acquired

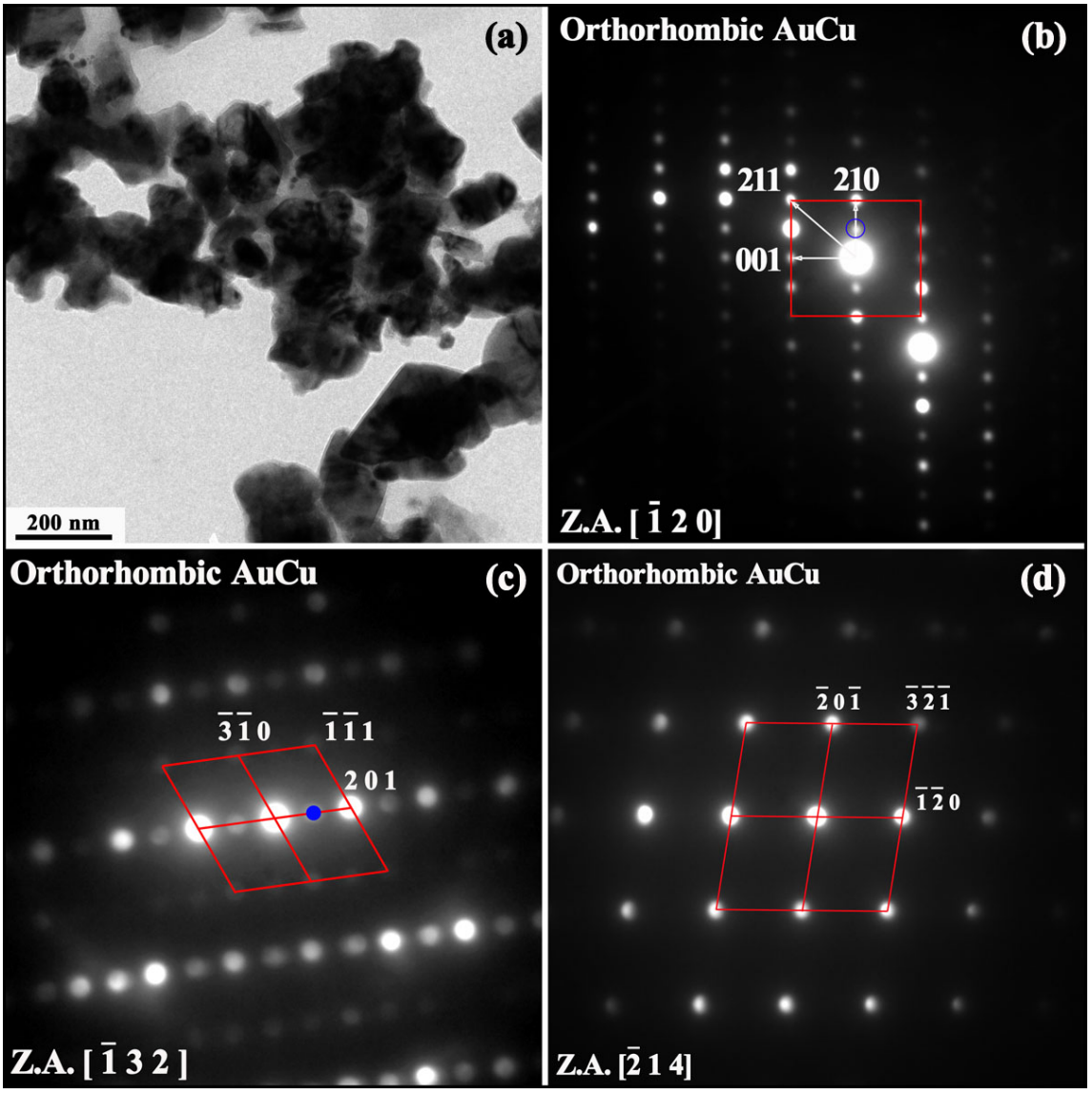

FIGURE 4.13: Representative BF TEM micrograph (a) and NBD patterns acquired from three different regions (b-d) from Au-Cu (1:1) sample. Blue open and filled circles in Figures (b) and (c) showing superlattice spots along [210] and [201] directions of orthorhombic AuCu oriented along [$\bar{1}$20] and [$\bar{1}$32] zone axes respectively. Figure (d) shows NBD and spots could be indexed as those of orthorhombic AuCu (oP8) phase along [$\bar{2}$14] zone axis.

NBDs have been substantiated by a set of computed diffraction patterns of orthorhombic AuCu (oP8) along the zone axes of [132], [$\bar{1}$32] , [$\bar{1}$20] and [$\bar{2}$14], respectively, and are presented in Figures 4.15 (a), (b), (c), and (d). In the experimentally observed diffraction

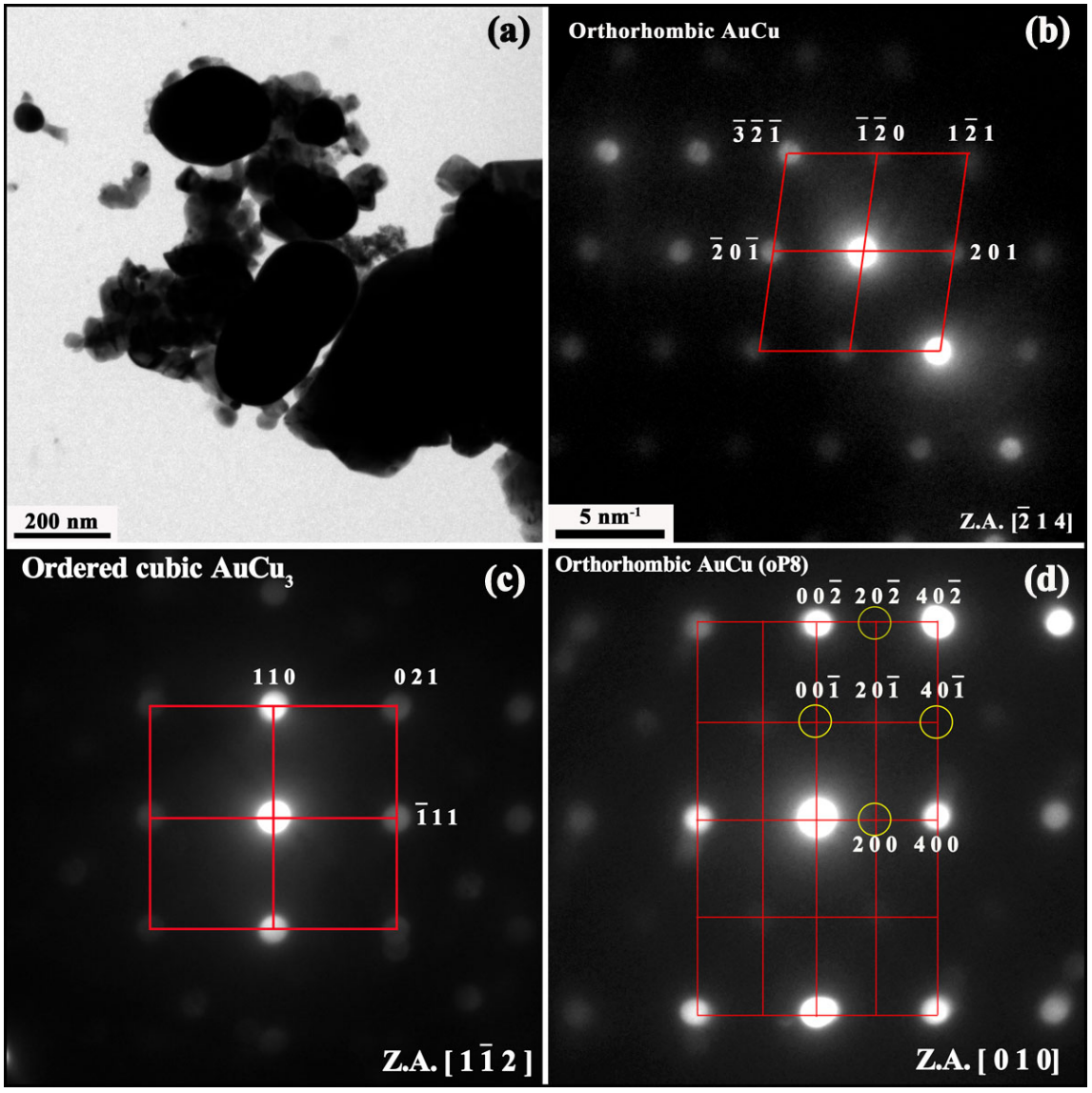

FIGURE 4.14: Representative BF TEM micrograph (a) and NBD patterns acquired from three different regions (b-d) from Au-Cu (1:3) sample. Figure 4.14 (b) and (d) could be indexed as orthorhombic AuCu with some of the extinct spots (shown as yellow open circles) in latter with zone axes [$\bar{2}$14] and [010] respectively. Figure 4.14(c) shows NBD and spots could be indexed as those of ordered cubic $AuCu_3$ along zone axis [1$\bar{1}$2].

patterns from [132], [$\bar{1}$32] , [$\bar{1}$20] zone axes, extra spots as marked in the Figures are observed. This necessarily means that the reciprocal lattice vectors along those directions are getting halved in comparison to the reported oP8 AuCu structure. Reduction of reciprocal lattice vectors may be attributed to either ordering of vacancies or chemical ordering. The ordered spots in the first three cases have been shown by blue spots along [3$\bar{1}$0], [201] and [210] directions. The simulated diffraction patterns along [$\bar{2}$14] resembles with that of oP8 AuCu along this zone. This shows that some of the regions have been transformed to standard oP8 AuCu and remaining display structural modifications based on oP8. Such type of ordering has been observed earlier based on oI40 basic cell [196, 197].

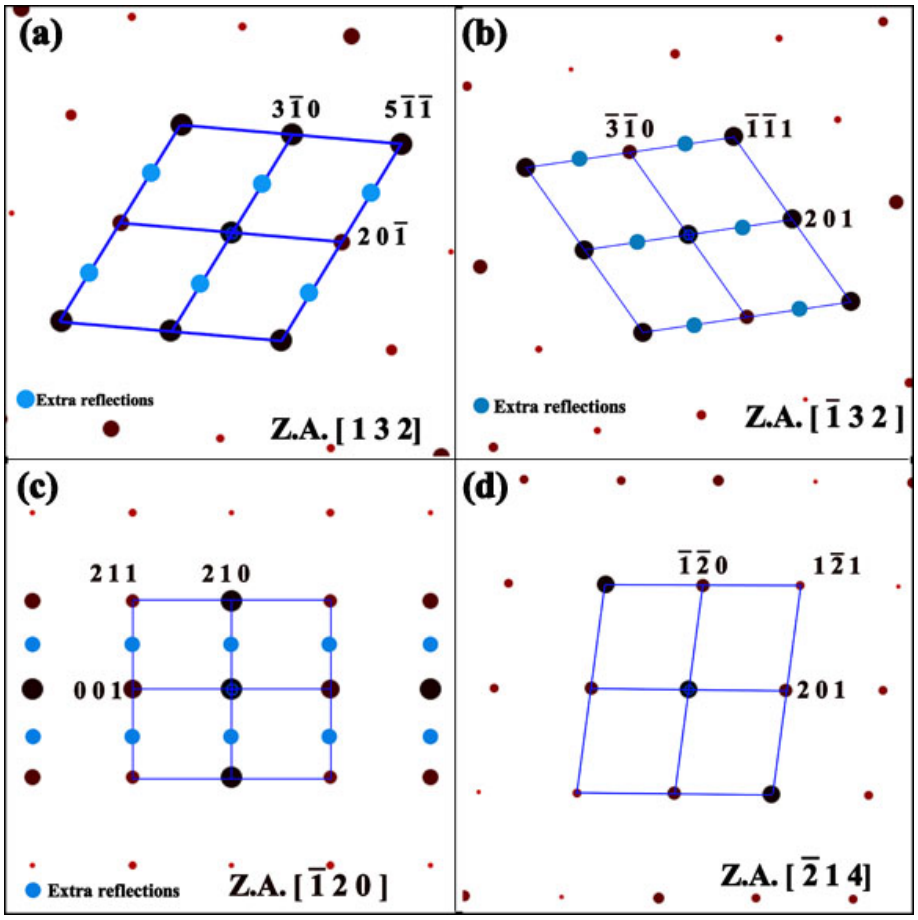

FIGURE 4.15: Computer generated DPs from orthorhombic AuCu (oP8) corresponding to experimentally acquired NBDs from Au-Cu samples.

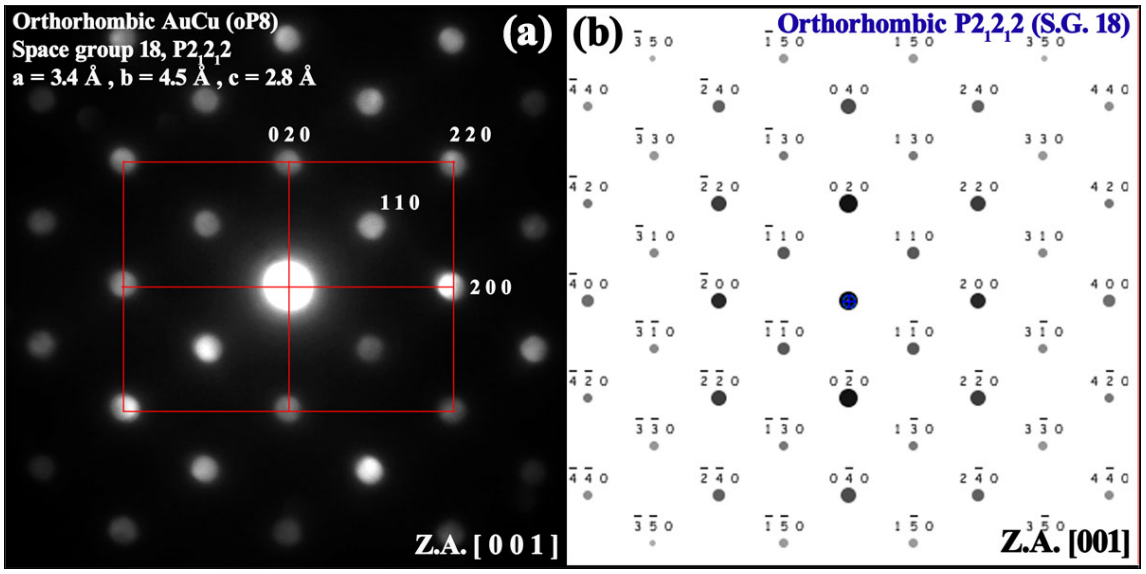

FIGURE 4.16: Experimental NBD pattern (a) and computed diffraction pattern corresponding to special Wyckoff positions of orthorhombic space group $P2_12_12$ (S.G. no. 18) (b).

In the NBD pattern shown in Figure 4.12 (c), all the spots could not be indexed based on standard oP8 cell in $[\bar{1}04]$ zone. The closest spots as indicated in blue color remained unindexed. The diffraction pattern led us to conclude that one is dealing with a new structure. This will be termed as type-I structural modification of oP8. One of the choices could be arrived at by invoking group-subgroup relationship of the orthorhombic cell. The best choice has come out to be orthorhombic $P2_12_12$ (S.G. no. 18) with cell parameter of a $\sim$ 3.4 Å, b $\sim$ 4.5 Å, c $\sim$ 2.8 Å. The computed DP along [001] zone axis (shown in Fig. 4.16 (b)) has all the attributes of DP shown in Figure 4.16 (a). It may be noted that all the spots belong to this zone of the new cell and are indexed accordingly. The computed pattern in Figure 4.16 (b) has been arrived at based on the Wyckoff positions (2a and 2b) of the new structure $P2_12_12$ (S.G. no. 18) (cf. Table 4.4). Such a cell conforms to reflection conditions h + k = 2n. The original oP8 cell (S.G. no. 55) has got an atomic

density of 0.07 atoms /Å^3. Ignoring the difference in radii of Au and Cu, one is expected to maintain such number density of even for cell of $P2_12_12$ (S.G. no. 18). However, this density comes out to be higher ($\sim$ 0.09 atoms /Å^3). These densities are arrived at by dividing the total number of atoms in the cell by their volumes. To conform to the density of the basic cell, one has to introduce concepts of ordering between Au and Cu atoms as well as that of vacancy. Such vacancies are important for nano-sized crystals and help one explains the newer structural transformations. It may be realized that such a transformed unit cell of $P2_12_12$ cannot be arrived at by mere shifting of the positions of Au and Cu atoms. Figures 4.17 (a) and (b) clearly demonstrate this. Transformation resulted in the change of cell parameters as well as space group symmetry. One of the possible ways to outline such a transformation may be resulting out of reconstructive transformation that proceeds by nucleation and growth. It is important to note that change in occupancies of Cu and Au in the transformed unit cell ($P2_12_12$) may violate the hard sphere model along [100] and [010] directions. As a consequence of this, metallicity of the resulting phase may get compromised. As noted earlier, all the spots of NBD shown in Figure 4.14 (d) could not be indexed based on oP8 AuCu. Following aforesaid explanation, one will be able to index the pattern with the cell parameter a $\sim$ 4.46 Å, b $\sim$ 2.83 Å, c $\sim$ 4.56 Å belonging to $P2_12_12$ (S.G. no. 18). This will be referred to as type-II modification of oP8.The zone axis comes out to be [001]. The cell is depicted in Figure 4.17 (c). The computed diffraction pattern (4.18 (b) of this cell along [001] zone axis reproduces experimentally observed NBD is shown in Figure 4.18 (a). The Wyckoff positions of the cell were taken similar to those shown in Table 4.4 for $P2_12_12$ (S.G. no. 18).

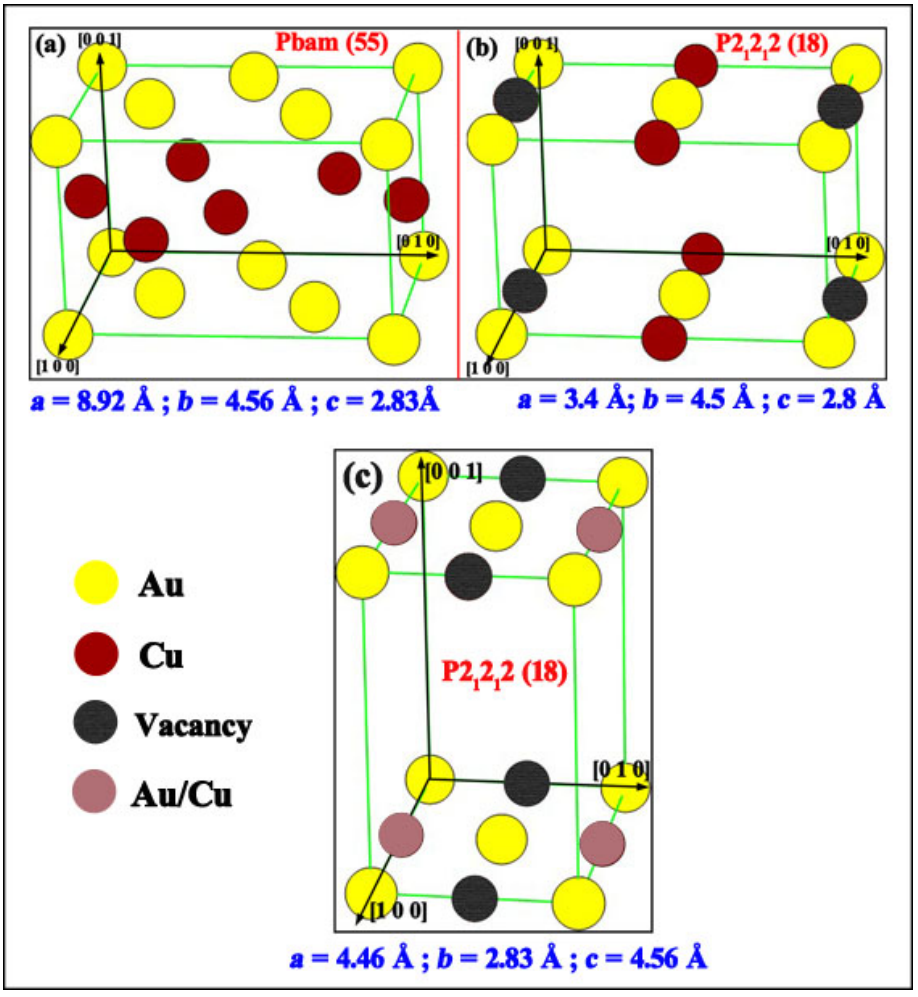

FIGURE 4.17: (a) Unit cell of standard orthorhombic AuCu (oP8) with shifted coordinates (for better illustration), (b) unit cell of transformed orthorhombic structure generated with space group $P2_12_12$ (S.G. no. 18) and (c) unit cell corresponding to transformed phase from orthorhombic Pbam to $P2_12_12$ with lattice parameters a = 4.46 Å, b = 2.83 Å, c = 4.56 Å.

TABLE 4.4: Orthorhombic space groups, their general and special Wyckoff positions and corresponding reflection conditions. The actual and transformed coordinates of orthorhombic AuCu (Space group Pbam; Space group no. 55) is given in columns IV and V.

Space group	**Wyckoff Positions**	**Coordinates**	**Standard Coordinates[1]**	**Transformed Coordinates after shift**	**Reflection conditions**
18,$P2_12_12$	2 b	0,½,z ½,0,-z	0, ½, 0 and ½ ,0,0 for Cu[1]	—-	h k 0: h + k = 2 n
	2 a	0,0,z ½,½,-z	0,0,0 and ½ , ½ ,0 for Au[1]		h k 0: h + k = 2 n
55, Pbam	4 h (Cu)	x, y, ½	0.662, 0.101, ½	0.479, -0.04, ½	0 k l: k = 2 n
		-x, -y, ½	0.338,0.899, ½	0.155, 0.758, ½	h 0 l: h = 2 n
		-x + ½, y +½, ½	0.838, 0.601, ½	0.655, 0.46, ½	h 0 0: h = 2 n
		x + ½, -y +½, ½	0.162, 0.399, ½	-0.021, 0.258, ½	0 k 0: k = 2 n
	4 g (Au)	x, y,0	0.183, 0.141, 0	0,0,0	—-
		-x,-y,0	0.817, 0.859, 0	0.634, 0.718, 0	
		-x + ½, y +½, ½	0.317, 0.641, 0	0.134, ½, 0	
		x + ½, -y +½, ½	0.683, 0.359, 0	½, 0.218, 0	
	4 f	0,½ ,z ; ½,0,-z	—-	—-	h k 0: h + k = 2 n
		0,½,-z ; ½,0,z			
	4 e	0,0,z ; ½,½,-z	—-	—-	h k 0: h + k = 2 n
		0,0,-z ; ½,½,-z			

In contrast to the previous structural transformation, the atomic number density remains nearly equal but less than that of oP8. Figure 4.17 (b) has to have vacancies in the cell to incorporate density increase to conform to original oP8 cell. Figure 4.17 (c) must have a vacant position at 0,1/2,0 position. The density decreases significantly to yield open structure. Thus, vacancy ordering is taking place in both the cases. The average chemistry of the samples was estimated by STEM-EDS. The average composition of Au for Au-Cu (3:1), Au-Cu (1:1) and Au-Cu (1:3) is estimated to be $\sim$ 54 at.%, 42 at.% and 69 at.% respectively. Average chemistry of the samples after heat-treatment got modified compared to those of as-synthesized samples. The chemistry of aforesaid phases in a localized region could not ascertained through STEM-EDS investigation in this study. The structural transformation from FCC AuCu to ordered orthorhombic AuCu

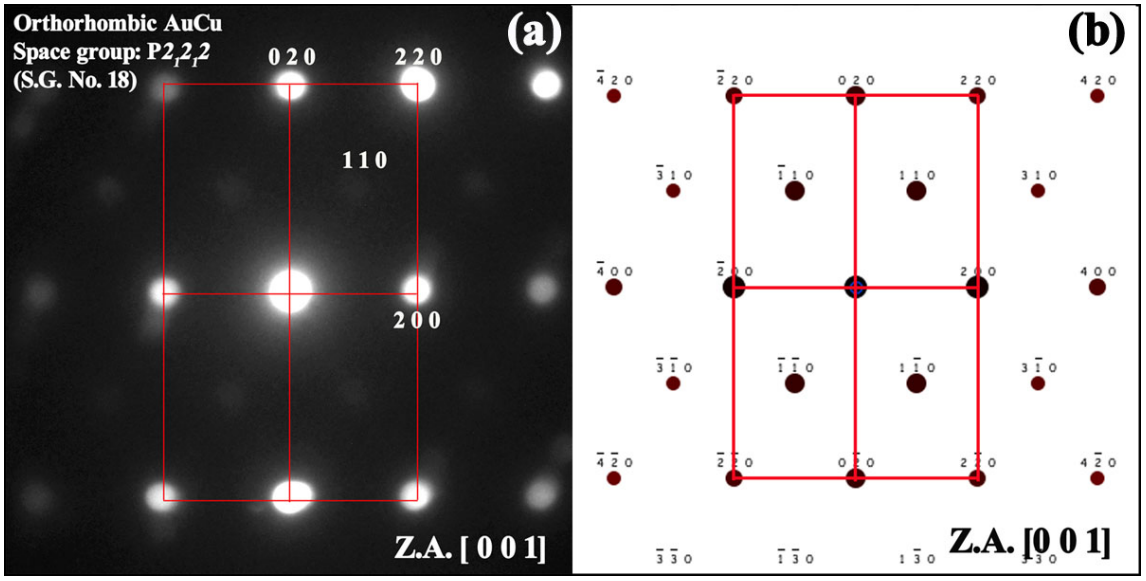

FIGURE 4.18: Experimental NBD (a) and corresponding computed patterns (b) from Au-Cu (1:3) sample. Figure (a) displays NBD indexed with space group $P2_12_12$ (S.G. no. 18) with lattice parameters a = 4.46 Å, b = 2.83 Å and c = 4.56 Å along [001] zone axis. The computed pattern corresponding to this cell (b) reproduces all the observed spots of (a).

(oP8) observed after heat-treatment for 1 h at $\sim$ 400 ^{o}C in this investigation is in contrast to more frequently observed ordered orthorhombic AuCu (oI40) phase reported in literature [197, 198]. It is important to realize that despite compositional differences in the Au-Cu samples, the observation of orthorhombic AuCu (oP8) and its related transformations in all three samples is counterintuitive. One can attribute this to the formation of kinetically constrained intermediate ordered orthorhombic AuCu (oP8) phase owing to inadequate duration of heat-treatment. In addition to that, as synthesized Au-Cu nanoparticles possess varied compositions of Au and Cu leading to compositional fluctuations among the particles. Further, long-range diffusion appears to be less likely in this study due to small size of the particles. The formation of intermediate phases in nanomaterials have already been deliberated in literature for several systems [61, 67]. For example, Williams and Johnson [67], demonstrated formation of a new metastable $NiSb_3$ compound using the modulated elemental reactant method. They further commented that $NiSb_3$ was only kinetically stable, as it transformed into the thermodynamically stable phases $NiSb_2$ and Sb upon annealing above 250 ^{o}C. The order-disorder transformation is well known in the Au-Cu system. Out of the two orthorhombic phases of Au-Cu reported in literature, oI40 is often observed. The lattice parameters of this phase are a =3.962 Å, b= 39.74 Å, c= 3.659 Å; ICDD card no. 05-001-0068 with space group: Imam (space group no.74). This has a fundamental pseudo tetragonal sub-cell a = b/10. This phase seems to exist between 385 ℃ and 410 ℃. However, our heat-treatment at 400 ^{o}C for 1 h in N_2 atmosphere gave rise to a structure based on oP8 with ordering along [210], [201] and [3$\bar{1}$0] directions. This observation is akin to those of one dimensional long period

superstructures in Au-Cu system [197, 198]. The ordering along [210], [201] and [$3\bar{1}0$] might take place due to systematic presence of vacant layers in these directions leading to change of periodicities in these directions. Microstructural evolution seems to have taken place to reduce surface energy. Hence, the resulting morphologies are identical. In this process however, the content within the nano-domain does not alter much. So, the point defects like chemical ordering or vacancies continue to be in that domain. By analogy therefore, one has to propose that surface energy minimization gives rise to changes in microstructural features whereas defects inside the domain leads to change in nature of coordination polyhedra resulting in structural phase transformation. Both of these are taking place concurrently during the process of heat-treatment. The equilibrium phase diagram for nano-sized system has to have a three dimensional construct even for binary system at constant pressure. It is known by binary equilibrium phase diagram that it has two-dimensional composition (abscissa) versus temperature (ordinate) plot. For dealing with structural phase transformation and phase stability in nanostructures one has to take care of the size as an additional axis. Thus, this will open a new direction of phase diagram studies. Findings reported in this chapter suggest that defects in the interior of nano-size domain can give rise to additional phase transformations at nano-scale. Such defects do introduce lot of local minima corresponding to newer phases hitherto unknown in microscopic domains of materials. Such a phase will get stabilized owing to kinetic barrier existing between two local minima.

4.2.4 Conclusions

The Ag-Cu alloy NPs were synthesized utilizing rice-starch as stabilizer by two step chemical reduction in ambient conditions. The XRD analyses reveal FCC (Ag) phase with maximum solid solubility of Cu $\sim$ 11 at.% and FCC (Cu) phase with maximum solid solubility of Ag $\sim$ 2.0 at.% respectively. Apart from FCC (Ag), presence of 2H-Ag phase is seen. The alloying behavior has been understood through HRTEM and HAADF-STEM-EDS. LSPR peaks of sols displayed absorbance corresponding to (Ag) NPs and (Cu) NPs. Sols stabilized with rice-starch is found to be stable for more than 2 months as assessed by LSPR peak position λ_{max} as a function of time. It is believed that this work will be important for plasmonic, interconnect, biomedical, photophysical, and photochemical applications. The stability of sols is an additional attributes of this investigation.

Rice-starch stabilized Au-Cu alloy NPs with varied morphologies such as wire like and short nanochains etc., could be synthesized by changing precursors proportions. TEM and STEM-EDS results show that Au-Cu alloying has taken place. The wire like nanostructures grown in Au-rich sample could be understood by oriented attachment of particles. Structural transformation in Au-Cu alloy nanoparticles after heat treatment at $\sim$ 400 ^{o}C for 1 h have been demonstrated. A series of one dimensional superlattice structures based on ordered orthorhombic AuCu (oP8) phase after heat treatment of Au-Cu nanoparticles at $\sim$ 400 ^{o}C for 1 h has been observed. They refer to ordering along [3$\bar{1}$0], [210] and [201] directions. Structural transformation from Pbam to $P2_12_12$ seems to be missing in literature. These structural transformations have been understood by invoking the presence of vacancies within the nano-domains of the nanoparticles. In contrast

to this, surface energy minimization seems to have predominantly guided the growth of microstructures.